Available online at www.sciencedirect.com
SCIENCE DIRECT®
Journal of Volcanology and Geothermal Research 143 (2005) 69–88
Journal of volcanology and geothermal research
www.elsevier.com/locate/jvolgeores

The effect of magma flow on nucleation of gas bubbles in a volcanic conduit

Hélène Massol[a,*], Takehiro Koyaguchi[b]

[a]*Laboratoire IDES Interactions et Dynamique des Environnements de Surface, CNRS, Université Paris-Sud, Orsay 91405 Cedex, France*
[b]*Earthquake Research Institute, University of Tokyo, Yayoi, Tokyo 113-32, Japan*

Received 15 December 2003; accepted 1 September 2004

Abstract

We solve the dynamics of magma ascent and the kinetics of bubble nucleation and growth simultaneously, which allow us to predict bubble sizes and number densities under ascent conditions. As magma rises toward the surface, the pressure decreases and eventually becomes less than the solubility pressure. When the degree of supersaturation becomes great enough, bubbles nucleate. Nucleation will stop as the concentration of volatiles in the melt decreases due to growth of existing bubbles and hence the degree of supersaturation decreases. We show that a second nucleation event may occur just below the fragmentation level. Near that level, the degree of supersaturation continuously increases as the magma is rapidly decompressed. As a result, nucleation will not stop until fragmentation occurs. This second nucleation event should be taken into account when interpreting bubble size distribution measurements made on natural pumices. The bubbles of the second nucleation event have high internal gas pressures up to 2 MPa greater than the liquid pressure, suggesting that the second nucleation event may enhance fragmentation of magma. We apply the model to the calculation protocol defined at the "Volcanic eruption mechanism modeling workshop, Durham, 2002". We found that as a result of disequilibrium degassing fragmentation occurs higher in the conduit than under equilibrium degassing.

Keywords: nucleation; magma; explosive eruption; viscosity; gas bubbles

1. Introduction

Eruptions involving a viscous magma are the most destructive and unpredictable volcanic events. These eruptions are explosive or effusive, mainly depending on the behavior of the gas phase within the magma. During ascent from the chamber to the surface, pressure decreases and the volatiles dissolved at depth exsolve to form gas bubbles. The flow regime is laminar until the gas volume fraction becomes high, and then the magma fragments and the flow becomes turbulent. This level is called the fragmentation level. The occurrence of fragmentation determines whether

* Corresponding author. Tel.: +33 1 69 15 61 40; fax: +33 1 60 19 14 46.
E-mail addresses: hmassol@geol.u-psud.fr (H. Massol), tak@eri.u-tokyo.ac.jp (T. Koyaguchi).

0377-0273/$ - see front matter © 2005 Elsevier B.V. All rights reserved.
doi:10.1016/j.jvolgeores.2004.09.011

the eruption is explosive or effusive. Previous numerical models already investigated a wide range of processes occurring within the conduit and involving the gas phase (Toramaru, 1989; Wilson et al., 1980; Jaupart and Allègre, 1991; Massol et al., 2001; Melnik, 2000; Papale, 2001; Mastin, 2002).

In order to better understand important features of volcanic eruptions such as change in eruptive style or the interpretation of geophysical measurements, it is necessary to couple magma flow with more microscopic processes occurring during magma ascent, such as nucleation of bubbles and crystals or the mechanism of fragmentation. The dynamics of bubble growth, such as the evolution of gas volume fraction, bubble size distribution, and gas overpressure before and after fragmentation have been widely studied from this point of view (Sparks, 1978; Navon et al., 1998; Proussevitch and Sahagian, 1996; Thomas et al., 1994; Kaminski and Jaupart, 1997). Sparks first showed in his pioneering work (Sparks, 1978) that gas overpressure can be built inside bubbles during ascent of highly viscous magmas (Wilson et al., 1980), and this idea has been supported by recent experimental and theoretical studies on bubble growth (Navon et al., 1998; Proussevitch and Sahagian, 1996; Gardner et al., 1999; Mourtada-Bonnefoi and Laporte, 2002). Nucleation of bubble is another key process which controls the behavior of the gas phase in conduits (Toramaru, 1989). Whether and how deep in the conduit nucleation occurs control the vesiculation dynamics, and hence influence the explosivity of an eruption (Mangan et al., 2004). Two end-members of nucleation exist at present; those are homogeneous nucleation that requires high volatiles supersaturation in the melt and heterogeneous nucleation on crystals or any solid surface that requires less supersaturation. It has also been suggested that some molecular scale heterogeneities or region in melts with crystal-like structure may aid heterogeneous nucleation. Recent publications (Mourtada-Bonnefoi and Laporte, 2002) pointed out that in the case of homogeneous nucleation in rhyolitic magmas, no nucleation occurs even for melts containing up to 4 wt.% water, suggesting that wide variations in the degree of disequilibrium degassing may contribute to the observed diversity of the eruption dynamics. In this study we focus on the interplay between (1) nucleation and growth of bubbles and (2) decompression due to magma ascent. We model the ascent dynamics of a viscous magma by solving simultaneously bubble nucleation and growth together with magma flow submitted to given boundary conditions at the bottom and top of the conduit. Such an approach allows us to assess whether degassing occurs at equilibrium and the effects on bubble pressures and ascent dynamics in general. Furthermore, because bubble growth is explicitly taken into account, bubble size is calculated as an output of the model.

In the following sections, we first describe the theory and the calculation method. Next, we show results and differences from the chemical equilibrium case. The effects of homogeneous or heterogeneous nucleation are investigated by varying effective surface tension in the calculations. The effects of nucleation and growth of bubbles on the process of fragmentation are studied by applying the different criteria available at present (i.e. critical gas volume fraction, critical strain rate (Papale, 1999), and stress around bubble (Zhang, 1999)) to our model. Finally we briefly discuss some geological implications, particularly from the viewpoint of resultant bubble size distribution.

The aim of this paper is not to reproduce exactly a true eruption but rather to understand: (1) what are the differences introduced by a non-equilibrium degassing in terms of magma ascent dynamics and the implications for eruptive processes, and (2) to predict, to a first order, bubble-size distributions that can be measured on natural eruptive products (i.e. pumices).

2. Governing equations

Magma ascends from the top of the magma chamber to the surface driven by the pressure difference between the chamber and the surface. During ascent, pressure decreases and the volatiles dissolved at depth exsolve to form gas bubbles. We calculate the dynamics of one-dimensional steady flow of the gas–liquid mixture through a cylindrical conduit of constant radius between the magma chamber and the surface and simultaneously the decrease in dissolved water and change of viscosity in the melt with nucleation and bubble growth at each step.

2.1. Macroscopic dynamics

In this study, we adopt the simplest model for the flow of gas–liquid mixture (e.g. Wilson et al., 1980); at first, the mixture consists of continuous liquid phase with gas bubbles (bubbly flow), and then the magma fragments to form a mixture of continuous gas phase containing liquid magma fragments (gas–pyroclast flow). The flow regime is laminar in the bubbly flow and turbulent in the gas–pyroclast flow. We assume the same velocity for the gas and liquid phases; the mixture is considered to be compressible and homogeneous moving at vertical velocity w. The vertical position z varies from zero at the top of the chamber to H, the height of the conduit. Our model is one-dimensional, where radial pressure and velocity do not vary across the conduit.

By averaging the mass and momentum conservation in both the liquid and gas phases and by adding the contribution of each phase, we obtain respectively:

$$\frac{\mathrm{d}(\rho w)}{\mathrm{d}z} = 0, \tag{1}$$

and

$$\rho w \frac{\mathrm{d}w}{\mathrm{d}z} = -\frac{\mathrm{d}P_\mathrm{m}}{\mathrm{d}z} - \rho g - F_\mathrm{fric}, \tag{2}$$

where ρ is the magma density, P_m is the mean pressure of the magma (gas–liquid mixture), and g is gravitational acceleration. Here F_fric is the force due to wall friction. Before fragmentation, F_fric is given as

$$F_\mathrm{fric} = \frac{8\mu Q}{\rho \pi a^4}, \tag{3}$$

where μ is the magma (bubble+liquid) viscosity, Q is the mass flux of the eruption, and a the conduit radius (Wilson et al., 1980, e.g.). After fragmentation, F_fric becomes:

$$F_\mathrm{fric} = \frac{f}{4a}\rho w^2, \tag{4}$$

where f is the coefficient related to conduit roughness, typically taken to equal 0.01 (Wilson et al., 1980).

As will be described below, the gas pressure inside the bubbles P_g is greater than the melt pressure P_l (i.e. pressure in the liquid phase) because of viscous resistance against bubble growth and surface tension (Sparks, 1978). The mean pressure in Eq. (2) is given as

$$P_\mathrm{m} = (1-\epsilon)P_\mathrm{l} + \epsilon\left(P_\mathrm{g} - \frac{2\sigma}{R}\right) \tag{5}$$

where ϵ is the gas volume fraction within the magma, σ the surface tension coefficient and R the bubble radius. Difference between this formulation and a one phase model formulation has been developed by Prud'homme and Bird (Prud'homme and Bird, 1978) and is given in Appendix A.

During ascent, the gas phase expands and the density decreases according to:

$$\rho = (1-\epsilon)\rho_\mathrm{l} + \epsilon\rho_\mathrm{g}, \tag{6}$$

where ρ_l is the liquid density (2400 kg/m^{-3}) and ρ_g is the gas density. In this paper we assume that the gas phase behaves as an ideal gas, namely,

$$\frac{P_\mathrm{g}}{\rho_\mathrm{g}} = R_\mathrm{g}T, \tag{7}$$

where R_g is the gas constant (462 J kg^{-1} K^{-1} for H_2O gas). It is also assumed that the temperature change due to expansion is negligible because of the large heat capacity of the liquid magma; T is set at 1123 K in our calculations.

2.2. Nucleation and growth of gas bubbles in magmas

As a magma rises, the pressure of the magma decreases and becomes less than the solubility pressure of water. When the degree of supersaturation becomes large enough, bubbles nucleate. Bubbles grow in the magmas during ascent because of diffusion of the water molecules dissolved in the melt and because of decompression. Generally, the gas pressure is not equal to the liquid pressure in the magma. Furthermore, if chemical equilibrium is not attained, the concentration of volatile species in the melt is not equal to the concentration at the bubble–melt interface (Proussevitch et al., 1993a). All these processes are taken into account in the bubbly flow regime by applying the cell model (cf. Proussevitch et al., 1993a; Melnik, 2000). The bubbly magma is approximated by an aggregate of bubble cells, with each bubble being surrounded by a concentric shell of incompressible melt. After fragmentation, we neglect

further individual bubble expansion and further water exsolution.

Fig. 1 summarizes the relationship between the pressure and the concentration of water during the processes of nucleation and growth of bubbles for one given pressure condition during ascent. The solubility curve of water in a magma is expressed as (Burnham, 1979).

$$C = sP^{1/2}, \tag{8}$$

where C and P represent the mass fraction of dissolved water in the liquid phase and the pressure, respectively, and s is the saturation constant (4.11×10^{-6} $Pa^{1/2}$ for silicic magmas).

Let us consider a liquid magma at a pressure P_l which contains an amount of dissolved water C_m (A_4 in Fig. 1). It is useful to introduce two points on the solubility curve; those are $A_1=(C_m, P_s)$ and $A_2=(C_s, P_l)$. At the stage of nucleation, point $A_4=(C_m, P_l)$ deviates from the solubility curve because a certain amount of supersaturation is needed for nucleation to occur. At that stage, the relationship between the water concentration in the liquid and the gas pressure within the newly nucleated bubble (defined as P_g^* hereafter) is represented by position A_1 (i.e. $P_g^*=P_s$).

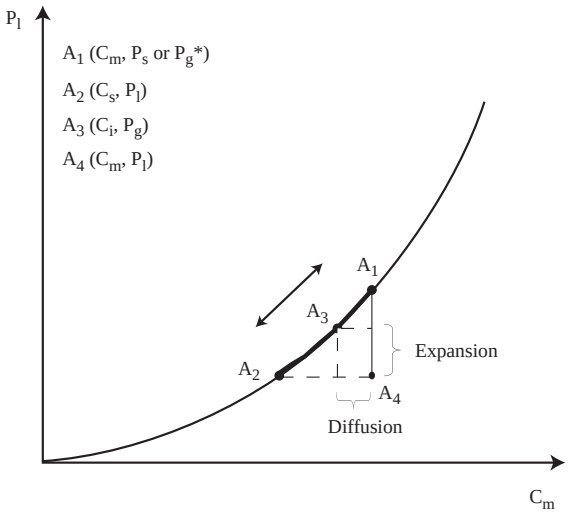

Fig. 1. (a) Schematic view of the processes of bubble growth. Below the solubility curve the dot represents one potential position of the magma during ascent on the (C_m, P_l) plot. When $A_3(C_i, P_g)$ is near A_1, expansion is the dominant mechanism, when $A_3(C_i, P_g)$ is near A_2, diffusion is the main mechanism.

The nucleation rate is controlled by the degree of supersaturation, that is, the distance between A_4 and A_1.

When a bubble is growing, the relationship between water concentration in the liquid and the gas pressure at the bubble–liquid interface is represented by position $A_3=(C_i, P_g)$ on the solubility curve between A_1 and A_2. The two main driving forces for bubble growth are expressed by the relationship between the position of A_3 and A_4. One driving effect is diffusion that advects volatiles toward the bubble due to the concentration difference C_m-C_i. It is represented in Fig. 1 by horizontal lines. The other effect contributing to bubble growth is expansion due to the outer pressure decrease. This effect is represented by vertical lines P_g–P_l in Fig. 1. These two effects (diffusion and expansion) are not independent as P_g evolves due to diffusion of volatiles toward the gas bubble. The interplay of the two processes during evolving ascent conditions (decreasing pressure) determines the position of A_3.

Strictly speaking, the solubility curve represents an equilibrium relationship under the condition where the gas pressure is equal to the liquid pressure. Therefore, the position of (C_i, P_g) may slightly deviate from the solubility curve because of the difference between the gas and liquid pressures. When the pressure difference between liquid and gas is rigorously taken into account, the water concentration in the liquid at the bubble–liquid interface is given by

$$C_i = C_{eq}\exp\left[\frac{v_m\left(P_g - P_l\right)}{2kT}\right] \tag{9}$$

where C_{eq} is the equilibrium water concentration at $P=P_g$ (i.e. the point exactly on the solubility curve), v_m the volume occupied by one molecule of water in the liquid (3×10^{-29} m^3) and k is the Boltzman constant (1.38×10^{-23} $J\,K^{-1}$) (Toramaru, 1989, 1995). Because of the small value of the volume of water molecule in the liquid, the difference between C_i and C_{eq} is negligible.

2.2.1. Nucleation of gas bubbles

Bubbles can nucleate when the melt becomes supersaturated in volatiles. The nucleation rate is defined by the number of nuclei of critical sizes per unit volume per unit time. Hurwitz and Navon, 1994

modified the classical nucleation theory (Hirth et al., 1970) for nucleation of water in magmas to give,

$$J = \frac{2n_0^2 v_m D}{a_0}\left(\frac{\sigma}{kT}\right)^{1/2}\exp\left\{-\frac{\Delta F^*}{kT}\right\}, \quad (10)$$

where ΔF^* is the free energy of formation of the nucleus, J is the nucleation rate, a_0 is the mean distance between two water molecules in the liquid, n_0 the concentration of volatiles molecules in the liquid and D is the diffusion coefficient. Toramaru (Toramaru, 1989, 1995) gave another expression of the nucleation rate based on the same basic theory; with a few developments, we find that both Eq. (10) and that of Toramaru give similar results of J. In this paper, we use Eq. (10).

In order to determine the nucleation rate J, we must evaluate ΔF^*. The minimum work of formation of a gas nucleus is equal to the variation of the Helmholtz free energy during the transition of a system containing only a melt phase to a system with a fluid nucleus within the melt. The variation of free energy of the system before and after the formation of the gas bubble is (see (Hirth et al., 1970; Mourtada-Bonnefoi, 1998)):

$$\Delta F = -\left(P_g^* - P_l\right)V_g + \left(\mu_{wg} - \mu_{wl}\right)N_{wg} + \sigma A, \quad (11)$$

where μ_{wg} and μ_{wl} are the chemical potentials of water in the fluid and in the melt, respectively, and V_g, A, and N_{wg} are the volume, surface area, and number of molecules in the nucleus, respectively. The work of formation is composed of three terms. The first is the energy needed for vaporization and is negative as the pressure in the nucleus is greater than the pressure in the melt (i.e. $P_g^* > P_l$). The second term is the energy due to supersaturation, and it is zero because it is assumed that the chemical potentials are equal in the melt and in the nucleus at equilibrium during nucleation (i.e. $\mu_{wg} = \mu_{wl}$). The third term is positive because it corresponds to the needed energy to create an interface. This function "work of formation" has a maximum for a critical radius of bubbles after which the energy needed for the formation decreases. The critical radius is obtained for, $\partial(\Delta F)/\partial R = 0$, and hence,

$$R_c = \frac{2\sigma}{P_g^* - P_l}, \quad (12)$$

bubbles greater than this critical radius can grow.

The free energy of formation of a nucleus ΔF^* depends on whether nucleation is homogeneous or heterogeneous. In the case of homogeneous nucleation, substituting Eq. (12) into Eq. (11), the free energy of formation is:

$$\Delta F^* = \frac{16\pi\sigma^3}{3\left(P_g^* - P_l\right)^2}. \quad (13)$$

Heterogeneous nucleation of bubbles in magma is defined as the development of a gas phase at the contact with a solid phase (crystal or conduit walls for instance). It requires less supersaturation than homogeneous nucleation. The value of the work of bubble formation depends on the geometry of the solid surface where the gaseous nucleus appears. In the case of a plane interface and a spherical nucleus, the mechanical equilibrium gives the following relation (Fig. 2) (Landau and Lifshitz, 1958):

$$\sigma_{gs} = \sigma_{ls} + \sigma_{gl}\cos\theta. \quad (14)$$

The work of formation of a nucleus of critical size on a solid surface is:

$$\Delta F^* = \frac{16\pi\sigma_{gl}^3}{3\left(P_g^* - P_l\right)^2}\Psi, \quad (15)$$

with

$$\Psi = \frac{(1+\cos\theta)^2(2-\cos\theta)}{4}. \quad (16)$$

If the liquid is highly wettable on the solid, the angle θ goes to 180° and Ψ goes to 0. Hence, no extra energy (super saturation) is needed for nucleation. Such a crystal favors nucleation, and vice versa. In this study we take the effect of heterogeneous nucleation by changing effective surface tension (i.e. $\sigma_{gl}\Psi^{1/3}$ in Eq. (15)).

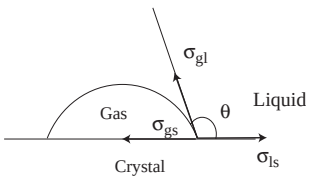

Fig. 2. Heterogeneous nucleation of a bubble on a plane liquid–solid interface (after Navon and Lyakhovsky, 1998). Coefficient σ_{gl}, σ_{gs} and σ_{ls} are respectively the gas–melt, the gas–solid and the liquid–solid interfacial surface tension. Angle θ is the wetting angle.

Knowing the nucleation rate, we calculate the evolution of the number of bubbles during ascent. The number of bubbles M_0 evolves as:

$$\frac{dM_0}{dz} = \frac{J}{w}, \tag{17}$$

w being the ascent velocity (Toramaru, 1995).

2.2.2. Bubble growth

Before fragmentation, the magma is modeled as a mixture composed of bubbles surrounded by a liquid shell. We assume that once nucleation occurs the bubbles are equally spaced in the liquid phase. As was mentioned above, there are two main driving forces for bubble growth. One driving effect is diffusion that advects volatiles toward the bubble due to the concentration difference between C_m the dissolved water content in the liquid and C_i the dissolved water concentration at the bubble–liquid interface. The present model does not take into account the detailed profiles of diffusivity coefficient or viscosity around the bubbles within the shells. The number of volatile molecules in a bubble, N_b, increases with the diffusional flux to the bubble. If the Peclet number $Pe \ll 1$ then a steady profile of water content is achieved with C_m being a representative dissolved water content in the melt and not a water content at a specific position within the liquid shell. The volatile flux from the melt toward the bubble is then a first order approximation and we suppose that:

$$\frac{dN_b}{dz} = \frac{4\pi RD}{w}\left(\frac{C_m - C_i}{1-\epsilon^{1/3}}\right), \tag{18}$$

with C_m being dissolved water concentration in the melt, C_i the dissolved water concentration at the bubble–liquid interface, R the bubble radius and ϵ the gas volume fraction. The factor $1-\epsilon^{1/3}$ in the above equation comes from the boundary condition $C=C_m$ at the boundary of the "bubble cell" (see Proussevitch et al., 1993a for the details of the "bubble cell" model). The melt volatile concentration decreases because of advection of volatile molecules toward the gas bubbles as (Toramaru, 1995):

$$\frac{dC_m}{dz} = -M_0\frac{dN_b}{dz} - N_b\frac{dM_0}{dz}. \tag{19}$$

The Peclet number might become equal or greater than one if ascent is fast near the fragmentation level. We will nevertheless make the above approximation keeping in mind that at greater Peclet numbers the melt will become more oversaturated than predicted by our model.

The other effect contributing to bubble growth is expansion due to the outer pressure decrease (P_g–P_l in Fig. 1). The expansion of the bubble in a viscous liquid is governed by the Rayleigh–Plesset equation (Plesset and Prosperetti, 1977),

$$\frac{dR}{dz} = \frac{R}{4\mu_l w}\left[(P_g - P_l) - \frac{2\sigma}{R}\right], \tag{20}$$

where μ_l is the viscosity of the surrounding melt. The surrounding melt viscosity is determined experimentally by Hess and Dingwell (Hess and Dingwell, 1996) as a function of dissolved water content. The gas pressure is a function of the number of molecules in the bubble and for an ideal gas is equal to:

$$P_g = \frac{N_b kT}{(4/3)\pi R^3}. \tag{21}$$

This equation is equivalent to Eq. (7). The gas volume fraction in the melt, ϵ, can be determined from M_0 and R by,

$$\epsilon = \frac{M_0(4/3)\pi R^3}{1 + M_0(4/3)\pi R^3}. \tag{22}$$

We do not know a priori if only one nucleation event occurs during ascent. If a decrease in nucleation rate is followed by an increase, we consider that a new population of bubble appears. For each of the populations, the radii of the new bubbles are averaged with the radius of the already growing bubbles. For different populations, we integrate different sets of bubble growth equations. In this case, the melt volatile concentration evolves as:

$$\frac{dC_m}{dz} = -\sum_i M_{0i}\frac{dN_{bi}}{dz} - \sum_i N_{bi}\frac{dM_{0i}}{dz}, \tag{23}$$

where the subscript i defines each bubble population. There are different gas pressures for each bubble population and the mean pressure is:

$$P_m = (1-\epsilon)P_l + \sum_i \epsilon_i\left(P_{gi} - \frac{2\sigma}{R_i}\right), \tag{24}$$

where $\epsilon_i = V_{gi}/\left(1+\sum_i V_{gi}\right)$, $\epsilon = \sum_i \epsilon_i$ and V_g being the gas volume.

2.3. Fragmentation criterion

The level of fragmentation is where the flow of magma undergoes a transition from a laminar flow of viscous bubbly liquid to a turbulent flow of gas carrying liquid fragments. One of the first hypotheses to explain the process of fragmentation was that the foam is not stable above a critical gas volume fraction which represents the close packing limit of spheres inside a liquid (Sparks, 1978). The condition of magma fragmentation is then given by:

$$\epsilon > \epsilon_{\mathrm{crit}}, \tag{25}$$

where ϵ_{crit} is the critical gas fraction and it is representatively 0.75 (Proussevitch et al., 1993b). On the other hand, recently, several other hypotheses are put forward to explain the fragmentation of magma. These hypotheses are based on the fracture mechanics; namely, whether magma fragments is determined by whether stress or strain rate around bubbles exceeds a critical value (Papale, 1999; Zhang, 1999). In this study we adopt two more criteria as follows.

Papale (Papale, 1999) proposes a strain rate criterion based on whether the magma crosses the brittle–ductile transition and behaves like a solid. The transition between the ductile and brittle behavior of the magma is given by the Maxwell relation (Maxwell, 1867; Papale, 1999):

$$\frac{\mathrm{d}w}{\mathrm{d}z} > \kappa \frac{G_\infty}{\mu} \tag{26}$$

where G_∞ is the elastic modulus at infinite frequency. Coefficient κ is determined experimentally (Dingwell and Webb, 1989; Webb and Dingwell, 1990) and its value is 0.01. The elastic modulus is found to be in the range of 2.5–30 GPa (Papale, 1999). The magma will break when the stress cannot be dissipated by viscous flow.

Zhang (Zhang, 1999) proposes a brittle-breakage based criterion; magma fragments when the stress around bubbles exceeds the tensile strength of the magma. The condition of magma fragmentation for this criterion is given by

$$\tau^{\mathrm{tt}} = \left(P_{\mathrm{g}} - \frac{2\sigma}{R} - P_{\mathrm{m}}\right)\frac{1+2\epsilon}{2(1-\epsilon)} - P_{\mathrm{m}} > S, \tag{27}$$

where τ^{tt} is the tangential stress around the bubble and S is the tensile strength of the magma. Experimentally, Webb and Dingwell (1990) and Romano et al. (1996) find strength values of order of 4 MPa for water-bearing silicate glass.

We first investigate the effects of non-equilibrium degassing compared with equilibrium degassing. In order to do so, we use the simple "gas volume threshold criterion" (Eq. (25)) and study the other important parameters influencing nucleation. Then, we investigate the differences in flow variables introducing the criteria of Papale (Papale, 1999) (Eq. (26)) and Zhang (Zhang, 1999) (Eq. (27)).

2.4. Model setup

The above equations (Eqs. (1), (2) and (23)) are integrated using a 4th order Runge–Kutta, finite-difference scheme as well as equations (Eqs. (17),

Table 1
Table of input parameters

Figure number	Q (kg s^{-1})	σ (N m^{-1})	a (m)	Fragmentation criterion
3 (non-eq.), 5, 7	8×10^{6}	0.06	25	75%
3 (eq.)	4.7×10^{6}	–	25	75%
5, 9b, 10	5.35×10^{5}	0.06	10	75%
5, 9a	8.45×10^{7}	0.06	50	75%
5	1.72×10^{8}	0.06	60	75%
–	2.4×10^{8}	0.06	65	75%
–	3.15×10^{8}	0.06	70	75%
–	4.2×10^{8}	0.06	75	75%
–	1.3×10^{9}	0.06	100	75%
6	2.6×10^{7}	0.02	50	75%
–	2.7×10^{7}	0.03	50	75%
–	3.2×10^{7}	0.04	50	75%
–	4.6×10^{7}	0.05	50	75%
–	1.45×10^{8}	0.07	50	75%
4, 6, 11	1.85×10^{8}	0.075	50	75%
6	2×10^{8}	0.08	50	75%
7, 8	1.1×10^{7}	0.06	25	"Zhang criterion"
–	6.8×10^{6}	0.06	25	"Papale criterion"
8	8.4×10^{7}	0.06	50	"Zhang criterion"
–	1.6×10^{8}	0.06	60	"Zhang criterion"
–	3.9×10^{8}	0.06	75	"Zhang criterion"
–	1.2×10^{9}	0.06	100	"Zhang criterion"
–	8.3×10^{7}	0.06	50	"Papale criterion"
–	1.7×10^{8}	0.06	60	"Papale criterion"
–	4.2×10^{8}	0.06	75	"Papale criterion"
–	1.3×10^{9}	0.06	100	"Papale criterion"

In all calculations, $H=5000$ m, $\mu_0=5.8\times10^{4}$ Pa s, $x_0=4$ wt.%, $\Delta P=10$ MPa, $D=10^{-11}$ m^2 s^{-1}. Note that if $\sigma=0.02$ N m^{-1} for a homogeneous nucleation corresponds to a value of $\Psi=8\times10^{-3}$ in the case of heterogeneous nucleation appropriate to a very wetting fluid.

(18), and (20)) for the two populations of bubbles. The boundary conditions are: $P(0)=P_{\mathrm{lith}}+\Delta P$ and $P(H)=P_{\mathrm{atm}}$ or $w(H)=w_{\mathrm{chock}}$ where $w_{\mathrm{chock}}=(\mathrm{d}\rho/\mathrm{d}p)^{1/2}$, ΔP the overpressure in the magma chamber and H the conduit height. Lithostatic pressure ($P_{\mathrm{lith}}=\rho_s gH$) is calculated assuming that the density of the country rock ρ_s is 2400 kg/m^3. We calculate the main variables: w, P_m, M_{01}, M_{02}, N_{b1}, N_{b2}, R_1, R_2 and C_m by a Runge–Kutta scheme, then, ϵ is derived from Eq. (22); P_{g1} and P_{g2} are derived from Eq. (21) and finally P_l is deduced from Eq. (5). One can find in Appendix A a comparison between the different pressures when one uses a homogeneous compressible phase or a two-phase model. In this paper we use the two-phase model described in the previous sections.

To capture the nucleation process accurately, we need a fine grid of 10^{-3} m size increment over the conduit height. We checked that the results do not change below this resolution. The parameters used in the calculations are listed in Table 1.

3. Results

3.1. General features

We solve the above system of equations and evaluate the effects of non-equilibrium degassing assuming steady state conditions. Fig. 3 shows representative results for a rhyolitic magma of initial viscosity of 5.9×10^4 Pa s, containing 4 wt.% of initial dissolved water. In this example, the surface tension coefficient is set at 0.06 N m^{-1} (for the other parameters used see Table 1). It clearly shows that fragmentation takes place at a shallower level of the conduit than in the equilibrium exsolution case. In this example, there is more than 500 m difference for the

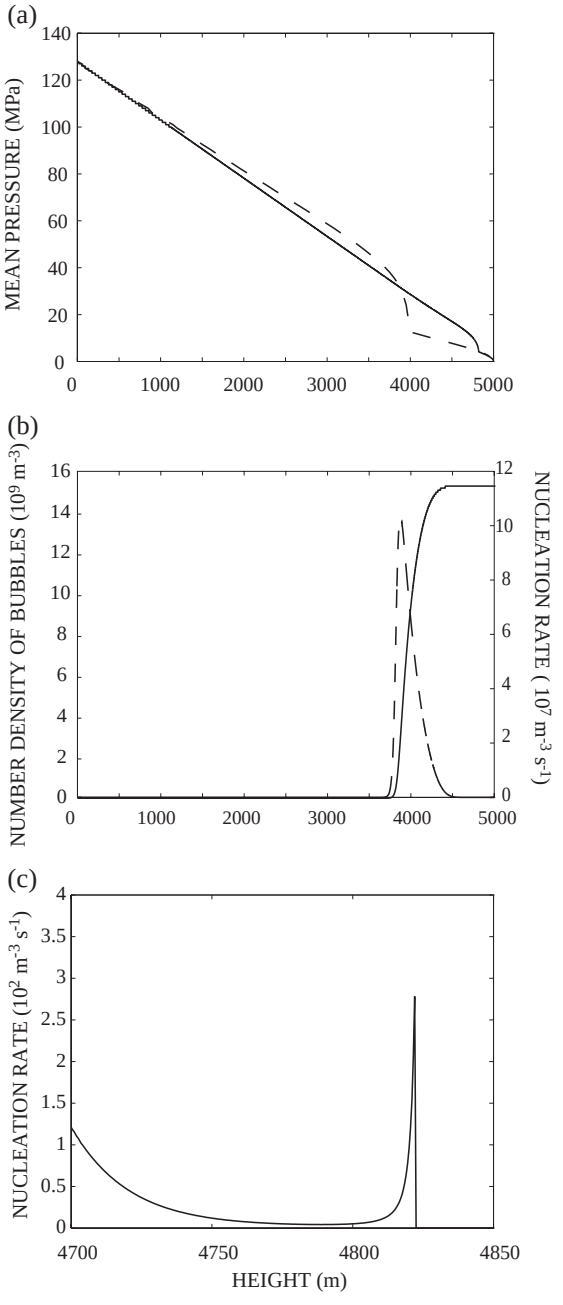

Fig. 3. (a) Evolution of mean pressure with height in the conduit. Mean pressure profile is compared with the pressure profile in the case of exsolution following the solubility curve, without nucleation, for the same magma (full stroke: non-equilibrium degassing, dashed stroke: equilibrium degassing). Note that fragmentation occurs higher in the conduit for non-equilibrium degassing. (b) Evolution of number density of bubbles (full stroke) and nucleation rate (dashed stroke) with height. Bubbles nucleate high in the conduit. Note that nucleation rate is almost a Dirac in that case. (c) Enlargement of the evolution of the nucleation rate with height near the fragmentation level. Note that it increases just before fragmentation. This increase is not visible in figure (b) because of a much lower order of magnitude of the second nucleation event compared to the first peak in this particular case. In this example fragmentation height is 4820 m. Parameters used in the calculation are listed in Table 1.

fragmentation height between the equilibrium and non-equilibrium cases. Indeed, for non-equilibrium degassing, the melt has to become sufficiently supersaturated in volatiles in order for bubbles to nucleate so that bubbles start to grow at lower pressure near the surface (see Fig. 3).

In this example, nucleation rate shows a very sharp peak function like a Dirac δ function (see Fig. 3b); a remarkable nucleation event occurs once and stops soon as the concentration of volatile in the melt decreases due to growth of existing bubbles. This behavior is consistent with the predictions by Toramaru (Toramaru, 1989). The present result, however, differs from previous studies on the basis of models with constant decompression rate; the nucleation rate increases again slightly just before fragmentation, although its magnitude is much lower than the first nucleation event (see Fig. 3c). Under certain conditions this nucleation event near the fragmentation level is more remarkable and shows another distinct peak of the nucleation rate (Fig. 4a and b). We call this nucleation event near the fragmentation level as second nucleation event hereafter. The second nucleation event has not been reported by any previous modelling studies on bubble nucleation and growth (Navon et al., 1998; Toramaru, 1995), and it is considered that this event is one of the most important consequences of the interplay between the dynamics of magma ascent and the kinetics of bubble nucleation and growth. However, continuous nucleation was thought as an explanation for bubble size distribution measured on pumices (Blower et al., 2001). In a following section, we present an example of the obtained size distribution obtained as an output of our calculation. The magnitude and timing of the second nucleation event as well as the first nucleation event should depend on geological parameters, such as conduit geometry (radius) and physical properties of magma (e.g. surface tension). In the following sections, we investigate the influence of these two parameters.

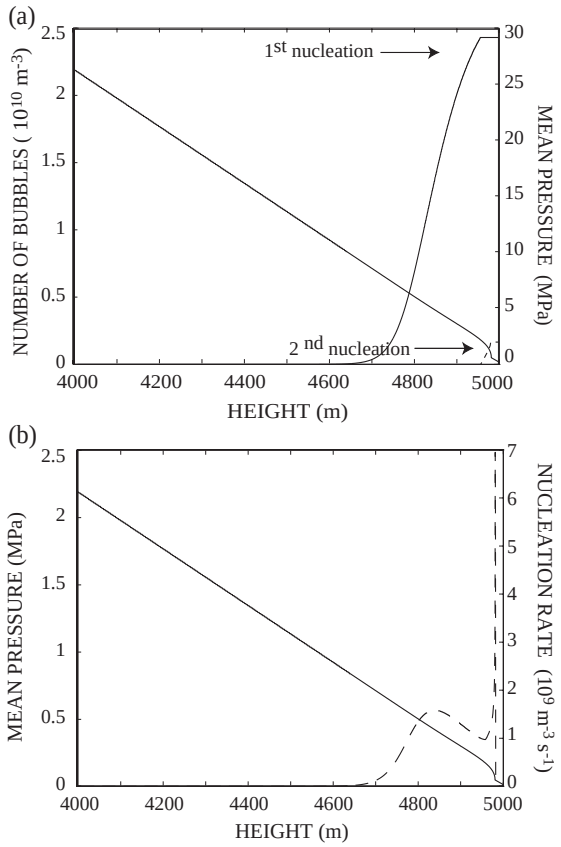

Fig. 4. (a) Evolution of the number of bubbles (full stroke: first population, dashed stroke: second population) and mean pressure (bold full stroke) with height in the conduit. Note that the second nucleation occurs again just before the fragmentation level. Parameters used in this calculation are listed in Table 1. (b) Evolution of the mean pressure (full stroke) and nucleation rate (dashed stroke) as a function of height in the conduit during ascent. Note the second nucleation peak that may trigger the fragmentation. Parameters for this calculation are listed in Table 1.

3.2. Influence of mass flux

Fig. 5 shows the number density of nucleated bubbles at fragmentation level, the bubble overpressure and the fragmentation height, as a function of the mass flux of the eruption for the same rhyolitic magma. In these calculations, mass flux increases, as conduit radius increases which decreases the friction term and promotes an increase in the ascent velocity. In turn, for a higher mass flux, the ambient pressure decreases a greater amount during a given time interval (i.e. decompression rate).

The results show that the number density of bubbles generated by the first nucleation (we call this "the first population" hereafter) increases as the mass flux increases (Fig. 5a). This tendency can be explained by the fact that the degree of supersatura-

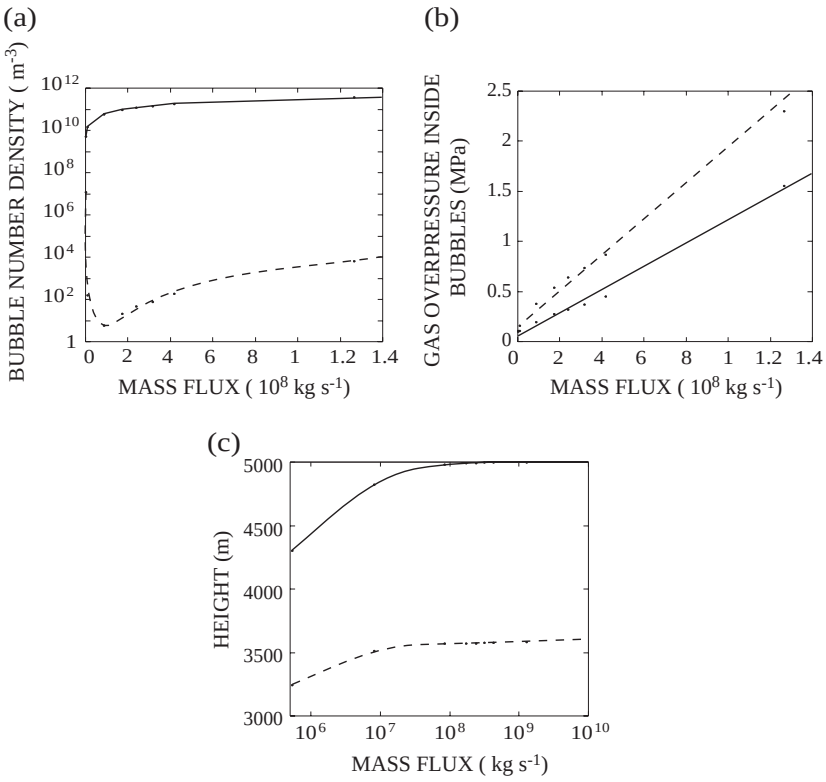

Fig. 5. (a) Bubble number density and (b) gas overpressure (full stroke: first population, dashed stroke: second population) as a function of mass flux of the eruption. (c) Fragmentation height (full stroke) and nucleation height (dashed stroke) as a function of mass flux of the eruption. Note that for all mass fluxes a second nucleation occurs. Parameters of these calculations are listed in Table 1.

tion, ($P_g^* - P_l$), and hence nucleation rate increases with the increase of decompression rate under higher mass flux conditions.

A similar tendency is also observed for the bubbles generated by the second nucleation (that we call "the second population" hereafter) except at very low mass flux conditions, where the melt can be highly supersaturated at the time of the second nucleation due to very low number of firstly nucleated bubbles (see Fig. 5a). Fig. 5b shows that the bubble overpressures increase as the mass flux increases. This tendency is particularly remarkable for the second population. This is also explained by the greater decompression rates at higher mass fluxes; the expansion of bubbles is limited due to rapid decompression, which results in the greater internal gas pressure.

Fig. 5c shows that both nucleation and fragmentation occur at shallower depths with increasing mass flow rates. The amount of supersaturation needed to nucleate bubbles depends on the initial dissolved water content and surface tension. Because we held both parameters constant, the mean pressure reached at the first level of nucleation is the same for all mass fluxes. As mass flux decreases, the mean pressure gradient dP_m/dz increases to balance the friction forces. The supersaturation pressure needed to trigger nucleation is then reached at shallower depths in the conduit when mass flow rate increases. The fragmentation depth depends on both the nucleation depth and on the expansion undergone by the nucleated bubbles up to the level of fragmentation. There are two competing effects as the mass flux increases: (1) the nucleation height increases, which increases the fragmentation height, and (2) the expansion of bubble is prevented which decreases the fragmentation height. In the range of parameters studied here, the first effect is dominant.

3.3. Influence of the interfacial surface tension

One of the most important parameters governing the magnitude of nucleation is the surface tension coefficient. In this section, we describe how this parameter affects the occurrence of nucleation and the magnitude of nucleation rate. As mentioned in Section 2.2, heterogeneous nucleation on crystals or microlites can reduce efficiently the amount of supersaturation needed to trigger nucleation. Unfortunately, precise measures of surface tension coefficient are scarce (Bagdassarov et al., 2000; Mangan et al., 2004). Navon and Lyakhovsky (1998) show that wetting angle strongly depends on the crystals; oxides have a very good wetting, whereas feldspars have almost no wetting. The wetting angle also depends on the composition of melt; the wetting angle and hence the effect of heterogeneous nucleation is thought to be more important in rhyolite melt than dacite melt (Mangan et al., 2004). In this study we take all of these effects into account by varying the effective surface tension from 0.02 N m^{-1} to 0.08 N m^{-1} (see Section 2.2 for its definition).

Fig. 6a and b shows the magnitude of nucleation rate versus the value of the surface tension coefficient for the bubbles generated by the first nucleation and those by the second nucleation, respectively. We recall that the higher the surface tension, the greater must be the supersaturation, and hence the initial pressure in the nucleus, to counterbalance the surface tension force. The nucleation rate is mostly controlled by the exponential term in Eq. (10). The evolution of J with respect to σ is then controlled by the evolution of ΔF^* with respect to σ. Calculating the derivative $d(\Delta F^*)/d\sigma$, one can find that the sign of this derivative depends on the relative magnitude of two terms: $d(\Delta P^*)/d\sigma$ and $3\Delta P^*/2\sigma$, with $\Delta P^* = P_g^* - P_l$. If $d(\Delta P^*)/d\sigma < (3\Delta P^*)/2\sigma$ then the nucleation rate should decrease with surface tension. Roughly, this is what is observed for the first population (Fig. 6a). For σ between 0.02 and 0.04 N m^{-1}, the decompression rate at the time of nucleation is almost constant and the nucleation rate evolves as $J_{max} \propto \sigma^{-4}$ which is compatible with Toramaru results (Toramaru, 1995) who found that $J_{max} \propto \sigma^{-4.5}$ in the "diffusion controlled regime". At other values of σ, the decompression rate at the time of nucleation increases with surface tension and the relationship between σ and J_{max} deviates from the linear decompression of Toramaru (1995). At $\sigma = 0.08$ N m^{-1} the flow is not fragmented, and the nucleation rate is limited by the exit boundary condition.

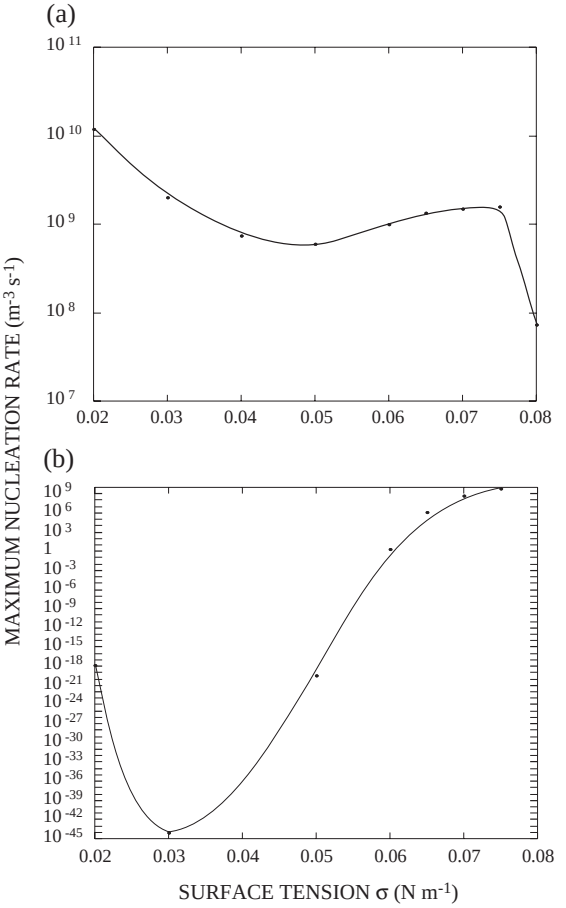

Fig. 6. (a) Maximum nucleation rate for the first nucleated population of bubbles. We stop the calculations when the surface tension reaches a value such that the magma does not fragment anymore. (b) Maximum nucleation rate for the secondly nucleated bubbles. The regime change occurring at $\sigma = 0.03$ N m^{-1} is due to the fact that increasing the surface tension leads to nucleate at lower ambient pressure. This in turn increases significantly the oversaturation. In all calculations, $H = 5000$ m, $a = 50$ m, $\mu_0 = 5.8 \times 10^{-4}$ Pa s, $x_0 = 4$ wt.%, $\Delta P = 100$ MPa, $D = 10^{-11}$ m^2 s^{-1}. Mass fluxes are between 2.6 10^7 kg s^{-1} and 2 10^8 kg s^{-1}.

For the second population (Fig. 6b) we observe a different trend. Below $\sigma = 0.03$ N m^{-1} the nucleation rate decreases with surface tension, then, at higher surface tension coefficient, the nucleation rate increases again. This is because, for high surface tension coefficient, the secondly nucleated bubbles

appear at shallower depth and smaller pressure. At this level, the decompression rate is large enough for the term $d(\Delta P)/d\sigma$ to dominate. Also we should note that unlike the first nucleation event, the second nucleation continuously increases until fragmentation (see Section 4.1), and is limited by the timing of fragmentation. When the relative timing between second nucleation and fragmentation are close, the second nucleation stops due to the occurrence of fragmentation before its rate increases. As the surface tension increases, the gas volume fraction of the first population at the time of the second nucleation decreases from $\epsilon = 74\%$ for $\sigma = 0.02$ N m^{-1} to $\epsilon = 45\%$ for $\sigma = 0.075$ N m^{-1}. In the above calculations we tentatively adopt the fragmentation criterion based on the critical gas volume fraction (i.e. Eq. (25)). Therefore, the smaller the surface tension is, the closer the timing of fragmentation is to that of the second nucleation. This effect also acts to increase the maximum rate of the second nucleation with increasing surface tension.

After a value of $\sigma = 0.075$ N m^{-1}, the magma does not fragment anymore but flows out the conduit as a lava dome. Experimentally, the surface tension value is estimated to be close to 0.1 N m^{-1} (Mangan and Sisson, 2000; Bagdassarov et al., 2000; Mourtada-Bonnefoi and Laporte, 2004). Because a magma containing 4 wt.% is likely to erupt explosively, we infer that heterogeneous nucleation should be common in nature. We also conclude that the variation of the degree of supersaturation due to the disequilibrium gas exsolution may play a role in the transition of eruption style from effusion one to explosion (Woods and Koyaguchi, 1994; Jaupart, 1992); however, this problem will not be considered further, because it is beyond the main scope of this study.

3.4. Influence of the fragmentation mechanisms

In the above calculations we adopt the fragmentation criterion based on the critical gas volume fraction (i.e. Eq. (25)); however, some of the quantitative features of our results also depend on applied fragmentation criteria mentioned earlier in Section 2.4. We call,

- "Papale criterion" when the strain rate exceeds a critical value ((Papale, 1999), Eq. (26)). Here we take a critical value of the elastic modulus of 2.5 GPa.
- "Zhang criterion" when gas pressure inside bubbles is high enough for the tangential stress to exceed the tensile strength of the magma ((Zhang, 1999), Eq. (27)). In this study, we take $S = 4$ MPa (Romano et al., 1996).

Fig. 7a shows the pressure drop and Fig. 7b the vesicularity on the last 1500 m of the conduit, near the fragmentation level for the two fragmentation criteria, for a magma with initial viscosity 5.9×10^4 Pa s and $\sigma = 0.06$ N m^{-1}. The results show that the two criteria

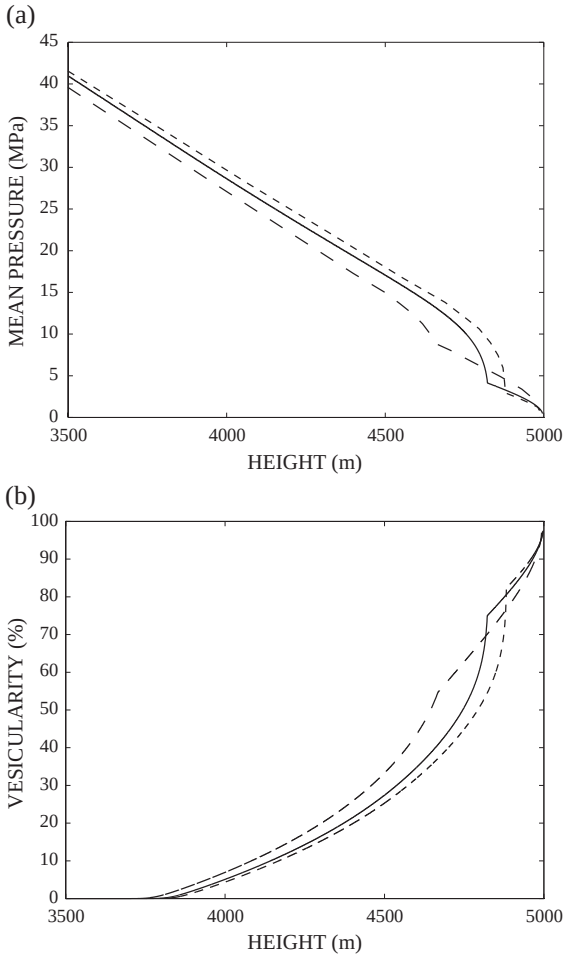

Fig. 7. (a) Evolution of mean pressure with height in the conduit for the three criteria (full stroke: gas volume fraction criterion, large dashed stroke: "Zhang criterion", small dashed stroke: "Papale criterion") and (b) Evolution of vesicularity with height. Note the differences in fragmentation height and vesicularity at fragmentation. Parameters for this calculation are listed in Table 1.

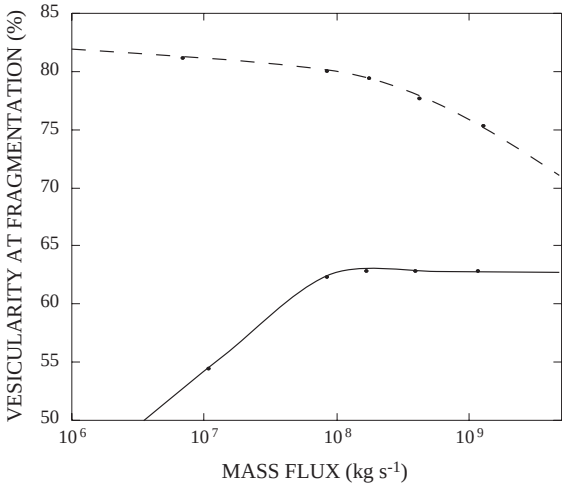

Fig. 8. Evolution of the vesicularity at fragmentation as a function of the mass flow rate of the eruption for the two criteria defined in the text. Note the opposite trends for "Zhang criterion" (full stroke) and "Papale criterion" ('dashed stroke'). Parameters for this calculation are listed in Table 1.

are not equivalent and there is a significant difference in terms of vesicularity at fragmentation. "Zhang criterion" leads to lower vesicularity at fragmentation than "Papale criterion". The build-up of critical overpressure occurs deep in the conduit, at high mean pressure (see Fig. 7a). Fig. 8 shows how vesicularity at fragmentation evolves with the fragmentation criterion considered as a function of mass flux. In the case of fragmentation only caused by the strain rate increase ("Papale criterion"), vesicularity decreases with mass flux. Because of the initially higher velocity for higher mass flux, the strain rate is then reached at lower gas content than for low mass flux. The vesicularity achieved at fragmentation is of order of 78% in that case. On the other hand, in the case of "Zhang criterion", the fragmentation is caused by an overpressure of order of 2 MPa within the secondly nucleated bubbles (see Fig. 4b). When the mass flux increases, the nucleation of new bubbles happens shallower in the conduit, therefore, the first population of bubbles has more time to grow. In that case, the vesicularity achieved at fragmentation increases with mass flux and varies between 50% and 62.5%. We recall that the model presented here is one-dimensional. Vesicularity is then, an average value across the conduit. It is likely that the vesicularity should also depend on the radial position of the erupted material within the conduit. However, we believe that the general trend for the evolution of vesicularity with respect to mass flux should not be modified.

For magma with high viscosities, the ascent rates are lower and hence the strain rates, such that the critical strain rate for fragmentation might not be achieved. The tensile stress failure ("Zhang criterion") might then be favored compared to "Papale criterion". The process of fragmentation may affect significantly the vesicularity and number bubble density measured in pumices.

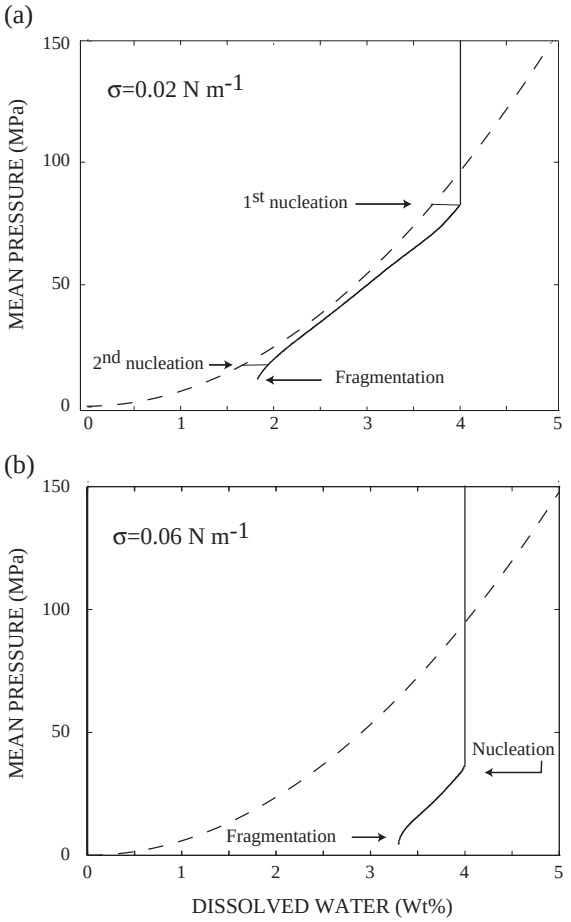

Fig. 9. (a) Evolution of dissolved water in the melt with decreasing pressure (full stroke) compared to the equilibrium solubility curve (dashed stroke). Note that near the fragmentation level the supersaturation increases again and triggers a secondary nucleation. (b) When surface tension coefficient is greater, nucleation happens shallower in the conduit at low ambient pressure and the "two nucleation events" happen very close from each other on a short vertical distance. Parameters used in this calculation are listed in Table 1.

4. Discussion

4.1. The second nucleation

In this section, we discuss the reasons why the second nucleation occurs. Fig. 9 shows the evolution of the amount of dissolved water in the melt compared to the saturation curve for two different values of surface tension ($\sigma = 0.02$ N m^{-1} and $\sigma = 0.06$ N m^{-1}). At first the pressure decreases and the supersaturation threshold is not reached, no bubbles nucleate and the water concentration in the melt remains constant. The nucleation is triggered when a sufficient amount of supersaturation is reached (indicated in Fig. 9 by the horizontal straight lines). After the first nucleation event, water is advected toward the bubble and the water concentration decreases in the melt such that nucleation stops. Then, when the melt accelerates near the fragmentation level, the decompression rate increases and the degree of supersaturation continuously increases with decreasing pressure (see Fig. 10). As pressure decreases, the solubility of water in the melt decreases rapidly, which also contributes to an increase the degree of supersaturation. These effects lead to new bubbles nucleating (Fig. 9), which does not stop until fragmentation criterion is reached. As mentioned in the previous section, the magnitude of this second nucleation peak is higher for higher surface tension coefficient (see Fig. 6b). Indeed, a higher surface tension leads to shallower nucleation depth.

Fig. 10 shows the decompression rate (Fig. 10a) and the deviation from the equilibrium state represented, respectively, by $P_s - P_l$ (Fig. 10b) and $C_m - C_i$ (Fig. 10c) as a function of height in the conduit. The decompression rate increases by more than two orders of magnitude near the fragmentation height. This large decompression rate corresponds to an increase in oversaturation represented both by an increase in $P_s - P_l$ and $C_m - C_i$ (see Fig. 10b and c). This effect was predicted to occur by Navon and Lyakhovsky, 1998. They found

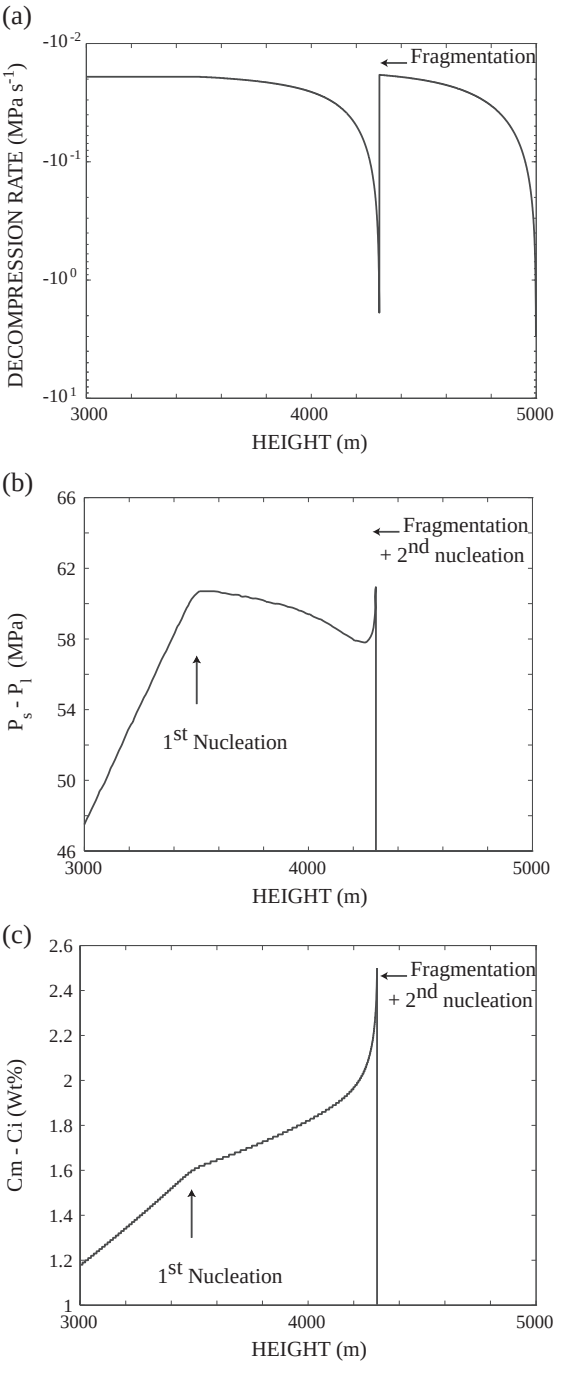

Fig. 10. Evolution of (a) decompression rate as a function of height in the conduit, (b) gas overpressure in the first population of bubbles, (c) difference between dissolved water concentration in the melt and at the liquid bubble interface in the last 2000 m of the conduit. The arrow "first nucleation" indicates the level where nucleation rate becomes significant ($J > 10^5$ m^{-3} s^{-1}). Note that both $C_m - C_i$ and $P_s - P_l$ increases as the decompression rate decreases sharply near the fragmentation level. The fragmentation level is also here just slightly above the level of secondary nucleation so that the two levels are not distinguishable at this scale. Note that the decompression rate has negative values so that large negative values mean large decompression rate. Parameters used in this calculation are listed in Table 1.

an oversaturation of 0.7 wt.% in volatiles in the upper part of the conduit for a liquid film thickness of 100 μm, and between 2 and 3 wt.% for a bubble separation of 1 mm when they apply a constant decompression rate of 3×10^{-2} MPa s^{-1}. This order of magnitude is below the decompression rate achieved at fragmentation in our case. In the case shown in Fig. 10 the bubbles radii at fragmentation are 519 μm and 76 μm and the number density 5.1×10^{9} m^{-3} and 1.25×10^{7} m^{-3} for the first and second population respectively. The mean radius can be estimated as: $R_{eq}=((M_{01}R_1^3+M_{02}R_2^3)/(M_{01}+M_{02}))^{1/3}$ and is equal here to 519 μm with the liquid film thickness being 571 μm. An oversaturation of order of 2.4 wt.% is compatible with the estimation of Navon and Lyakhovsky, 1998 given that the decompression rate is greater by at least one order of magnitude in this example. As was shown in Section 3, some quantitative features such as the magnitude and timing of the first and second nucleation events varies as a function of geological parameters and magma properties. The fact that the degree of supersaturation increases in the shallower part of conduit is, however, considered to be robust. It is suggested that the occurrence of the second nucleation would be common under reasonable conditions of explosive eruptions.

4.2. Geological implications

In this section, we attempt to estimate size distribution of bubbles at fragmentation. By calculating simultaneously bubble growth, nucleation, and magma ascent, we can predict the evolution of the mean radius for each bubble population as a function of depth in the conduit. In our calculation only two populations of bubbles are taken into account. For the first nucleation event this approximation is almost valid because the nucleation peak is roughly a Dirac δ function, because of advection of water toward the newly nucleated bubbles. On the contrary, the second nucleation event would be better explained by a continuous nucleation event.

Fig. 11a represents the evolution of bubble radius during ascent in one example. We use the gas volume fraction fragmentation criterion in this calculation because it falls between the two other criteria in terms of vesicularity at fragmentation. We recall that we initially average the radii of new and growing bubble for each of the bubble populations. We note that the evolution of bubble radius at the beginning of ascent follows the square root solution by (Navon et al., 1998). At that stage, the pressure gradient is almost linear and gas pressure follows closely the mean pressure such that we are under the long times experimental conditions of Navon et al. (1998). Then, because both expansion and diffusion are promoted by an increase in gas pressure and high ascent rate near fragmentation (see Figs. 1 and 9), bubble growth rate increases sharply until fragmentation occurs.

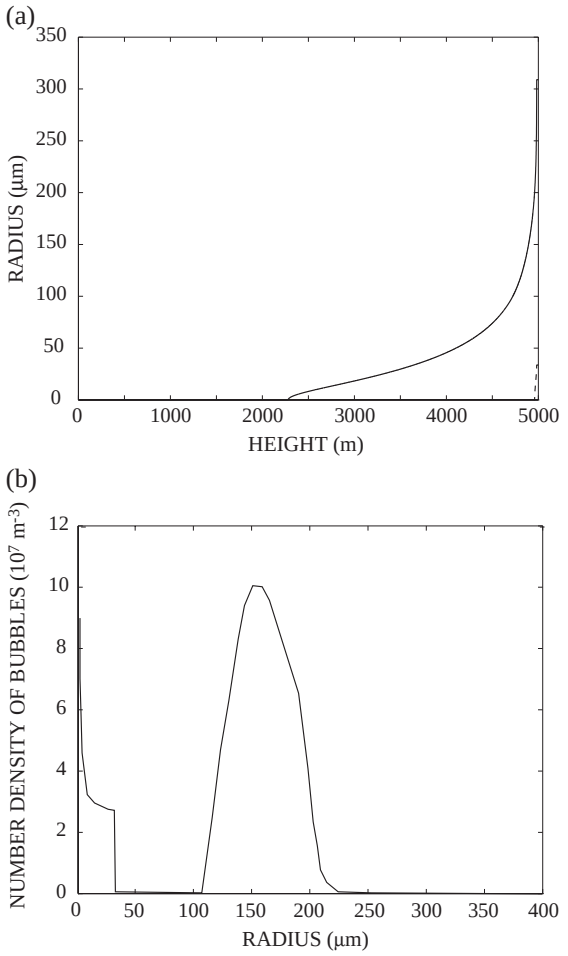

Fig. 11. (a) Evolution of bubble radius during ascent for the two population of bubbles (full stroke: first population and dashed stroke: second population). Note that the growth rate increases near fragmentation due to both effects of high decompression rate and high oversaturation. (b) Estimate of the size distribution at the fragmentation level. Note the fine population corresponding to tiny secondly nucleated bubbles. Parameters for this calculation are listed in Table 1.

As previously mentioned in Section 3.2, the final bubble radii reached at fragmentation depends on the ascent velocity. Under conditions of Section 3.2, for instance, for a mass flux of 5.3×10^5 kg s^{-1} the mean radii of the first and second populations of bubbles have values of 519 μm and 76 μm. For a higher mass flux of 1.26×10^9 kg s^{-1} the mean radii values are 120 μm and 6 μm for the firstly and secondly nucleated bubbles, respectively. This clearly shows that bubble growth is delayed more for faster ascent velocities. These values can be considered as a lower bound for bubble radii in pumices (considering the effect of expansion after fragmentation, or coalescence), but it is of the order of magnitude of measurements made on natural pumices. For instance, Sparks and Brazier (Sparks and Brazier, 1982) describe 3 populations centered on the respective values 1, 10 and 100 μm.

We now attempt to estimate bubble size distribution from our calculations. At each depth within the conduit, we know the nucleation rate and hence how many new bubbles are nucleated as well as the bubble growth rate from Fig. 11a. From the nucleation radius, we may hence infer a value of final size distribution at fragmentation. Here we average new nucleated bubbles over 5 m of conduit and calculate the final radii of these populations. Fig. 11b shows the number density of bubbles as a function of bubble radius corresponding to the calculated growth rate of Fig. 11a. This plot shows two peaks around 1 μm and 150 μm. The fine population corresponding to late nucleation event near the fragmentation level at large decompression rate and the coarser population being due to first nucleation and growth at depth in the conduit. At first order, it reproduces the observed multiple peaks measured in pumices by previous

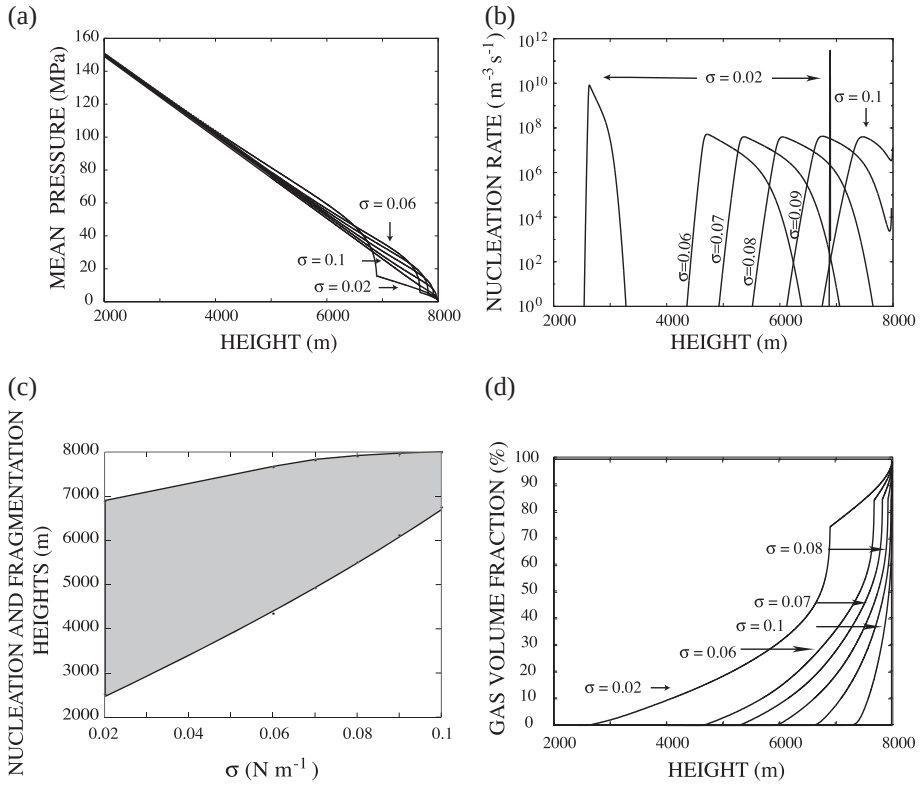

Fig. 12. Profiles showing the evolution of the main variables along the conduit height for different surface tension coefficients varying from $\sigma=0.02$ N m^{-1} to $\sigma=0.1$ N m^{-1}. For $\sigma=0.11$ N m^{-1} the magma is not fragmented. See Table 2 for calculation parameters. The fragmentation occurs deeper in the conduit for low surface tension coefficients decreasing from $\sigma=0.02$ N m^{-1} to $\sigma=0.1$ N m^{-1}. On Plot (c), the grey area defines the compressible section.

authors (Sparks and Brazier, 1982; Klug et al., 2002; Whitam and Sparks, 1986, e.g.). These peaks, mostly at 10, 100 or 1000 μm are interpreted whether due to coalescence or multiple nucleation. Here we show that multiple nucleation events during ascent is a possible explanation to account for the observed multiple peaks in bubble radii measurements. A possible explanation for not observing a 1 μm population in recent measurements (Klug et al., 2002; Whitam and Sparks, 1986) could be that these overpressured bubbles are involved in the process fragmentation.

Obviously, this prediction is not intended to reproduce field measurements exactly, but, it does provide an estimation of size distribution that can be tested against field data. This first attempt is, of course, incomplete because coalescence and expansion after fragmentation are not taken into account, but we find that to a first order it reproduces observed data.

5. Conclusions

Coupling the dynamics of magma ascent and the microscopic process of nucleation and growth of gas bubbles has several important implications for eruption dynamics.

- The nucleation rate may increase near fragmentation level, due to high decompression rate leading to supersaturation of the melt. As a result bubbles nucleate more than once in a volcanic conduit.
- Fragmentation height is roughly 1000 m shallower under non-equilibrium degassing than by considering equilibrium exsolution. Therefore, accurate predictions on fragmentation height should consider non-equilibrium degassing.
- Vesicularity at fragmentation is strongly dependent on the fragmentation process.
- The late nucleation of gas bubbles high in the conduit may trigger fragmentation. Indeed, the secondly nucleated bubbles have high internal pressures and, because of the large gas volume fraction due to the first population of bubbles, the velocity is high enough that the brittle transition can be achieved.
- Our model presents a first order estimate of bubble sizes at fragmentation, which can be compared with field data.

Acknowledgements

This work was supported by the JSPS grant P99729. Takehiro Koyaguchi was also supported by funds of Ministry of Education Science and Culture of Japan (Nos. 14080204 and 14540388) and Helene Massol by CNRS FRE 2566. The authors acknowledge NSF for financing the "Volcanic Eruption Mechanism Modeling Workshop" as well as Dork Sahagian and Alex Proussevitch who have organized it in New Hampshire. We thank Jim Gardner, Atsushi Toramaru and an anonymous reviewer for their careful and constructive reviews of the manuscript. Steve Sparks and Oded Navon are also acknowledged for their helpful comments on an earlier version of the manuscript. Helene Massol thanks Cinzia Farnetani for help and comments.

Appendix A

A.1. Workshop test case

We perform calculations according to the defined protocol in Durham in November 2002 using the model described in the previous section. For this set of calculations, we vary the diffusivity coefficient as a

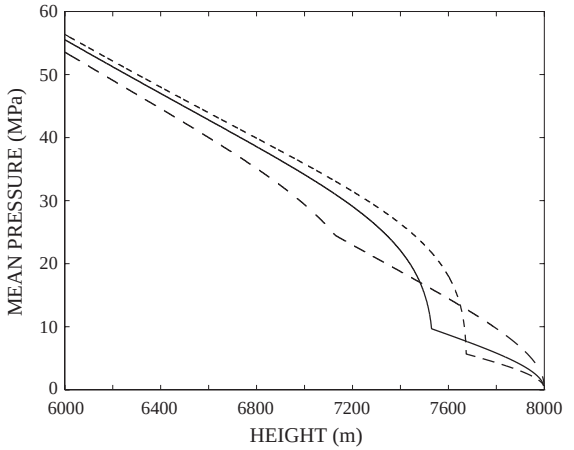

Fig. 13. Pressure profiles showing the evolution of the mean pressure for the three fragmentation criteria in the last 2000 m of the conduit (full stroke: gas volume fraction criterion, large dashed stroke: "Zhang criterion", small dashed stroke: "Papale criterion"). Parameters used for calculation are in Table 2. Note that again, fragmentation occurs at a greater pressure in the case of "Zhang criterion".

Table 2
Table of input parameters corresponding to the protocol calculations

Figure number	Q (kg s^{-1})	σ (N m^{-1})	Fragmentation criterion
12	5.9×10^6	0.02	"Papale criterion"
12, 13	5.7×10^6	0.06	"Papale criterion"
12	6.9×10^6	0.07	"Papale criterion"
–	9×10^6	0.08	"Papale criterion"
–	1.2×10^7	0.09	"Papale criterion"
–	1.6×10^7	0.1	"Papale criterion"
13	1.2×10^7	0.06	"Zhang criterion"
–	7.5×10^6	0.06	"75% gvf criterion"

In all calculations, x_0=5 wt.%, a=25 m, H=8000 m, μ_0=2.57 10^4 Pa s, ΔP=10 MPa.

function of the dissolved water water content in the melt (C_m) applying the diffusivity model of Zhang (Zhang and Behrens, 2000). The magma of rhyolitic composition contains 5 wt.% of dissolved H_2O and flows through a cylindrical conduit of 25 m radius and 8000 m height. The pressure at the bottom of the conduit is 200 MPa. The major parameter influencing the nucleation rate is σ, the surface tension coefficient. Fig. 12 show the pressure profile (a), nucleation rate profile (b), Fragmentation and nucleation depth (c) and gas volume fraction profile (d) for different surface tension coefficients from σ=0.02 N m^{-1} to σ=0.1 N m^{-1}. For all these calculations, the mass fluxes values are respectively between $Q=5.9\times10^6$ kg s^{-1} and $Q=1.6\times10^7$ kg s^{-1}. The viscosities reached at fragmentation are between 1.5×10^7 Pa s and 2.3×10^6 Pa s respectively between σ=0.02 N m^{-1} and σ=0.1 N m^{-1}. For σ=0.11 N m^{-1} the fragmentation did not occur and the bubbly section flowed out the vent. As previously shown, the fragmentation occurs much higher in the conduit than in the equilibrium case. At most the fragmentation depth is 1105 m below the surface, as shown in Fig. 12c. Because the nucleation rate depends highly on surface tension, the greater the surface tension the more difficult it is to nucleate bubbles and hence, the nucleation happens shallower in the conduit for higher surface tension coefficient (see Fig. 12a, b, c and d). Fig. 13 shows the pressure profiles for the three fragmentation criteria mostly used at present and described previously. For the three criteria, fragmentation depth is shallower than in the equilibrium case (Tables 2 and 3).

A.2. The different pressures

In this section, we want to compare the different pressures used in different two-phase flow formulations. The stress tensor has to be equivalent in the magma when using one or the other formulation. We call $\Pi_{1\phi}$ the stress tensor used when the magma is considered as a compressible equivalent mixture (Prud'homme and Bird, 1978), and $\Pi_{2\phi}$ in the two-phase flow formulation. For simplicity, we ignore the effect of surface tension in this appendix. The only components that change are the diagonal terms in the stress tensor. For the one phase mixture:

$$\Pi_{1\phi}rr = \Pi_{1\phi}\theta\theta = P_g - \lambda\frac{\partial w}{\partial z}, \tag{A.1}$$

and

$$\Pi_{1\phi}zz = P_g - \lambda\frac{\partial w}{\partial z} - 2\mu\frac{\partial w}{\partial z}. \tag{A.2}$$

Table 3
Table of results corresponding to the protocol calculations

Variable	σ=0.02 (pc)	σ=0.06 (pc)	σ=0.07 (pc)	σ=0.08 (pc)	σ=0.09 (pc)	σ=0.1 (pc)	σ=0.06 (zc)	σ=0.06 (gvf)
$w(0)$ (m s^{-1})	1.3	1.2	1.5	1.9	2.6	3.3	2.5	1.6
$w(H)$ (m s^{-1})	109	85.3	74.1	68.7	55.1	39.5	123	107
Q (kg s^{-1})	5.9×10^6	5.7×10^6	6.9×10^6	9×10^6	1.2×10^7	1.6×10^7	1.2×10^7	7.5×10^6
Fragmentation ves. (%)	73.4	82.6	84.4	84.2	84.1	82	49.4	75
Exit ves. (%)	98.9	98.6	98.1	97.3	95.4	91.7	98	98.6
M_{01} (m^3)	6.3×10^{11}	1.6×10^{10}	1.1×10^{10}	8.9×10^9	6.9×10^9	4×10^9	4.7×10^{10}	2.4×10^{10}
M_{02} (m^3)	2.2×10^{11}	0	0	0.2	1.7×10^4	10^7	0	0
R_1 (μm)	103	432	488	527	567	661	170	311
R_2 (μm)	26.2	–	–	37.3	37.4	48.7	–	–
Fragmentation depth (m)	1105	327	179	81	28	7	872	471

In all calculations, x_0=5 wt.%, a=25 m, H=8000 m, μ_0=2.57 10^4 Pa s, ΔP=10 MPa, pc means "Papale fragmentation criterion", zc means "Zhang fragmentation criterion" and gvf means "Gas volume fraction fragmentation criterion". Radii R_1 and R_2 are the mean radii of the two populations at the fragmentation level.

For the two-phase mixture:

$$\Pi_{2\phi} rr = \Pi_{2\phi} \theta\theta = (1-\epsilon)P_l + \epsilon P_g, \quad (A.3)$$

and

$$\Pi_{2\phi} zz = (1-\epsilon)P_l + \epsilon P_g - 2\mu \frac{\partial w}{\partial z}. \quad (A.4)$$

Equating the dynamic pressures (which is the third of the trace of the tensor), we obtain an expression for the second viscosity coefficient in the one phase formulation as a function of the mean pressure and of the gas pressure:

$$\lambda = \frac{P_g - P_m}{\nabla \cdot \vec{v}}. \quad (A.5)$$

We can also express the liquid pressure in terms of the bulk viscosity coefficient, K,

$$P_l = P_g - (K - 2/3\mu)\frac{\nabla \cdot \vec{v}}{1-\epsilon}, \quad (A.6)$$

with

$$K = \lambda + 2/3\mu, \quad (A.7)$$

where in our case, $\nabla \cdot \vec{v} = \frac{dw}{dz}$.

References

Bagdassarov, N., Dorfman, A., Dingwell, D.B., 2000. Effect of alkalis, phosphorus, and water on the surface tension of haplogranite melt. Am. Mineral. 85, 33–40.

Blower, J.D., Keating, J., Mader, H., Phillips, J., 2001. Inferring volcanic degassing processes from vesicle size distributions. Geophys. Res. Lett. 28, 347–350.

Burnham, C., 1979. Magmas and Hydothermal Fluids. Geochemistry of Hydrothermal Ore Deposits. J. Wiley and Sons, pp. 71–136.

Dingwell, D.B., Webb, S., 1989. Structural relaxation in silicate melts and non-Newtonian melt rheology in geological processes. Phys. Chem. Miner. 16, 508–516.

Gardner, J.E., Hilton, M., Carroll, M.R., 1999. Experimental constraints on degassing of magma: isothermal bubble growth during continuous decompression from high pressure. Earth Planet. Sci. Lett. 168, 201–218.

Hess, K.U., Dingwell, D.B., 1996. Viscosities of hydrous leucogranitic melts: a non-arrhenian model. Am. Mineral. 81, 1297–1300.

Hirth, J.P., Pound, G.M., St. Pierre, G.R., 1970. Bubble nucleation. Metall. Trans. 1, 939–945.

Hurwitz, S., Navon, O., 1994. Bubble nucleation in rhyolitic melts: experiments at high pressure, temperature, and water content. Earth Planet. Sci. Lett. 122, 267–280.

Jaupart, C., 1992. The Eruption and Spreading of Lava. Chaotic Processes in the Geological Sciences. Springer Verlag, New York, pp. 175–205.

Jaupart, C., Allègre, C.J., 1991. Gas content, eruption rate and instabilities of eruption regime in silicic volcanoes. Earth Planet. Sci. Lett. 102, 413–429.

Kaminski, E., Jaupart, C., 1997. Expansion and quenching of vesicular magma fragments in plinian eruptions. J. Geophys. Res. 102, 12187–12203.

Klug, C., Cashman, K.V., Bacon, C.R., 2002. Structure and physical characteristics of pumice from the climactic eruption of Mount Mazama (Crater Lake, Oregon). Bull. Volcanol. 64, 486–501.

Landau, L., Lifshitz, E., 1958. Statistical Shysics. Pergamon, New York.

Mangan, M., Sisson, T., 2000. Delayed, disequilibrium degassing in rhyolite magma: decompresssion experiments and implications for explosive volcanism. Earth Planet. Sci. Lett. 183, 441–455.

Mangan, M., Mastin, L., Sisson, T., 2004. Gas evolution in eruptive conduits: combining insights from high temperature and pressure decompression experiments with steady-state flow modeling. J. Volcanol. Geotherm. Res. 129, 23–36.

Massol, H., Jaupart, C., Pepper, D., 2001. Ascent and decompression of viscous vesicular magma. J. Geophys. Res. 106, 16223–16240.

Mastin, L.G., 2002. Insights into volcanic conduit flow from an open-source numerical model. Geochem. Geophys. Geosyt. 3 (1037).

Maxwell, J., 1867. On the dynamical theory of gases. Philos. Trans. R. Soc. Lond., A 157, 49–88.

Melnik, O., 2000. Dynamics of two phase conduit flow of high-viscosity gas-saturated magma: large variations of sustained explosive eruption intensity. Bull. Volcanol. 62, 153–170.

Mourtada-Bonnefoi, C., 1998. Thèse de Doctorat: Dynamique Thermochimique des Chambres Magmatiques et Vésiculation des Magmas Rhyolitiques. Université Blaise Pascal, Clermont Ferrand.

Mourtada-Bonnefoi, C., Laporte, D., 2002. Homogeneous bubble nucleation in rhyolitic magmas: an experimental study of the effect of H_2O and CO_2. J. Geophys. Res. 107 (2066) (ECV 2-1-19).

Mourtada-Bonnefoi, C., Laporte, D., 2004. Kinetics of bubble nucleation in a rhyolitic melt: an experimental study of the effect of ascent rate. Earth Planet. Sci. Lett. 218, 521–537.

Navon, O., Lyakhovsky, V., 1998. Vesiculation process in silicic magmas. The physics of Explosive Volcanic Eruptions, No. 145 in Geological Society Special Publication. The Geological Society, London, pp. 27–50.

Navon, O., Chekhmir, A., Lyakhovsky, V., 1998. Bubble growth in highly viscous melts: theory, experiments, and autoexplosivity of dome lavas. Earth Planet. Sci. Lett. 160, 763–776.

Papale, P., 1999. Strain-induced magma fragmentation in explosive eruptions. Nature 397, 425–428.

Papale, P., 2001. Dynamics of magma flow in volcanic conduits with variable fragmentation efficiency and nonequilibrium pumice degassing. J. Geophys. Res. 106, 11043–11065.

Plesset, M., Prosperetti, A., 1977. Bubble dynamics and cavitation. Annu. Rev. Fluid Mech. 9, 145–185.

Proussevitch, A.A., Sahagian, D.L., 1996. Dynamics of coupled diffusive and decompressive bubble growth in magmatic systems. J. Geophys. Res. 101, 22283–22307.

Proussevitch, A.A., Sahagian, D.L., Anderson, A.T., 1993a. Dynamics of diffusive bubble growth in magmas: isothermal case. J. Geophys. Res. 98, 17447–17455.

Proussevitch, A.A., Sahagian, D.L., Kutolin, V., 1993b. Stability of foam in silicate melts. J. Volcanol. Geotherm. Res. 59, 161–178.

Prud'homme, R.K., Bird, R.B., 1978. The dilatational properties of suspension of gas bubbles in incompressible Newtonian and non-Newtonian fluids. J. Non-Newton. Fluid Mech. 3, 261–279.

Romano, C., Mungall, J., Sharp, T., Dingwell, D., 1996. Tensile strengths of hydrous vesicular glasses: an experimental study. Am. Mineral. 81, 1148–1154.

Sparks, R.S.J., 1978. The dynamics of bubble formation and growth in magmas: a review and analysis. J. Volcanol. Geotherm. Res. 3, 1–37.

Sparks, R.S.J., Brazier, S., 1982. New evidence for degassing processes. Nature 295, 1–37.

Thomas, N., Jaupart, C., Vergniolle, S., 1994. On the vesicularity of pumice. J. Geophys. Res. 99, 15633–15644.

Toramaru, A., 1989. Vesiculation process and bubble size distributions in ascending magmas with constant velocities. J. Geophys. Res. 94, 17523–17542.

Toramaru, A., 1995. Numerical study of nucleation and growth of bubbles in viscous magmas. J. Geophys. Res. 100, 1913–1931.

Webb, S., Dingwell, D., 1990. Non-Newtonian rheology of igneous melts at high stresses and strain rates: experimental results for rhyolite, andesite basalt and nephelinite. J. Geophys. Res. 95, 15695–15701.

Whitam, A.G., Sparks, R.S.J., 1986. Pumice. Bull. Volcanol. 48, 209–223.

Wilson, L., Sparks, R.S.J., Walker, G.P.L., 1980. Explosive volcanic eruptions, IV. The control of magma properties and conduit geometry on eruption column behaviour. Geophys. J. R. Astron. Soc. 63, 117–148.

Woods, A.W., Koyaguchi, T., 1994. Transitions between explosive and effusive eruptions of silicic magmas. Nature 370, 641–644.

Zhang, Y., 1999. A criterion for the fragmentation of bubbly magma based on brittle failure theory. Nature 402, 648–650.

Zhang, Y., Behrens, H., 2000. H_2O diffusion in rhyolitic melts and glasses. Chem. Geol. 169, 243–262.